

Polarimetry and albedo of the Near-Earth Asteroid 2025 FA22

J.-P. Rivet¹, S. Bagnulo², P. Bendjoya¹, G. Borisov^{3,2}, A. Cellino⁴, M. Devogèle⁵, Z. Gray⁶, S. Ieva⁷, L. Kolokolova⁸, Y. G. Kwon⁹, A. Berdyugin¹⁰, S. V. Berdyugina^{11,12}, L. Boulanger¹, P. Fatka¹³, E. Frank², M. Lazzarin¹⁴, V. Piironen⁹, P. Pravec¹³, and the NEOPOPs team

¹ Observatoire de la Côte d'Azur, Université Côte d'Azur, CNRS Bd de l'Observatoire, CS 34229, 06304 Nice Cedex 4, France

² Armagh Observatory & Planetarium, College Hill, Armagh BT61 9DG, UK.

³ Institute of Astronomy and National Astronomical Observatory, Bulgarian Academy of Sciences, 72 Tsarigradsko Chaussée Blvd., BG-1784 Sofia, Bulgaria. e-mail: gborisov@nao-rozhen.org

⁴ INAF – Osservatorio Astrofisico di Torino, via Osservatorio 20, I-10025 Pino Torinese, Italy

⁵ ESA NEO Coordination Centre, European Space Agency, Largo Galileo Galilei, 1, Frascati, 00044, RM, Italy

⁶ Department of Physics, University of Helsinki, PO Box 64, 00014, Finland

⁷ INAF Roma

⁸ Department of Astronomy, University of Maryland, College Park, MD 20742-2421, US

⁹ Caltech/IPAC, 1200 E California Blvd, MC 100-22, Pasadena, CA 91125, USA

¹⁰ Department of Physics and Astronomy, FI-20014 University of Turku, Finland

¹¹ Istituto Ricerche Solari Aldo e Cele Daccò (IRSOL), Faculty of Informatics, Università della Svizzera italiana, Via Patocchi 57, Locarno, Switzerland

¹² Euler Institute, Faculty of Informatics, Università della Svizzera italiana, Via Buffi 13, 6900 Lugano, Switzerland

¹³ Astronomical Institute of the Academy of Sciences of the Czech Republic, Fričova 298, Ondřejov, CZ-25165, Czech Republic

¹⁴ INAF Padova

Received ; accepted

ABSTRACT

We report spectropolarimetric and broadband polarimetric observations of the near-Earth asteroid “2025 FA22” during its close approach of 18 September 2025 (about two Moon distances). The diameter of 2025 FA22 is estimated between 130 and 290 meters. It is among the largest NEAs observable at such proximity, prompting an International Asteroid Warning Network (IAWN) rapid-response campaign. Although early orbital solutions indicated a possible impact in 2089, further follow-up astrometric observations ruled out collision hazard. The favourable geometry of this close encounter enabled a dense coverage of the positive part of the phase-polarisation curve, from the high polarisation domain (high phase angles), nearly to the inversion angle where the linear polarisation rate vanishes. The spectropolarimetric observations provided the wavelength dependence of the polarisation rate. Using empirical relationships, an estimate of the geometric albedo could be drawn from the slope of the phase-polarisation curve at inversion angle. Moreover, the spectropolarimetric trends yielded constraints on the taxonomic class. These results demonstrate the interest of polarimetry and spectropolarimetry for rapid characterisation of newly discovered NEAs in planetary defence campaigns.

Key words. Asteroids: individual: (2025) FA22 – Polarization

1. Introduction

On 18 September 2025, the near-Earth asteroid (NEA) 2025 FA22 (hereafter FA22) had a close approach to Earth, reaching a minimum distance of about 2 lunar distances. With an estimated diameter between 130 and 290 m, FA22 is among the largest NEAs observed at such close range. Initially flagged as a possible impactor in 2089, and briefly topping ESA's Risk List¹, subsequent astrometric follow-up quickly refined its orbit and excluded any imminent impact scenario. Although FA22 poses no imminent hazard, its encounter presented a rare opportunity to carry out coordinated, multi-technique observations in the framework of the International Asteroid Warning Network (IAWN), a United Nations–endorsed consortium that coordinates global observations, data sharing, and communication on potential impact threats. In particular, the FA22 campaign was aimed at testing the planetary defence community's readiness to rapidly characterise a newly discovered NEA.

In this framework, polarimetry is particularly powerful. By measuring the linear polarisation of scattered sunlight as a function of phase angle (the angle between the target–Sun and target–observer directions), it is possible to derive key surface properties including albedo, regolith structure, and, when spectropolarimetric data are collected, also taxonomic classification (see Bagnulo et al. 2024 for a review).

Main-belt asteroids have been extensively studied with polarimetry, but geometrical constraints limit their ground-based observations to phase angles below 30 – 40°, where polarisation is small ($\lesssim 3\%$). Near-Earth asteroids, in contrast, can be observed at much larger phase angles where the fraction of linear polarisation becomes much higher, providing a golden opportunity to probe a mostly unexplored regime of the asteroid polarimetric behaviour, including a better understanding of the polarisation–albedo relationship. Such measurements are directly relevant for planetary defence: coupled with brightness measurements, albedo is a key parameter to obtain reliable estimates of an object's size. Moreover, surface properties inferred from po-

¹ <https://neo.ssa.esa.int/risk-list>

larimetric data influence the design and execution of any possible deflection attempt whenever this turns out to be needed.

Here we report spectro-polarimetric and filter-polarimetric measurements of FA22 obtained during its close approach. Our observing strategy exploited the brightness evolution of the object: spectro-polarimetry was carried out when FA22 was near its maximum brightness, enabling reliable measurement of the wavelength dependence of polarisation. Broadband filter polarimetry was used when the object was fainter, in order to efficiently sample the phase-polarisation curve with minimal telescope time.

For atmosphere-less bodies in the solar system, the phase-polarisation curve shows two distinct branches. At small phase angles, typically $\lesssim 20^\circ$, the flux polarized parallel to the scattering plane dominates the flux polarized perpendicularly; this is called the “negative branch”. At larger phase angles however, the flux polarized perpendicularly dominates, forming the “positive branch”. In our data set, we achieved dense coverage of the positive branch, starting just above the inversion angle α_0 (that separates the two branches) and extending up to the phase angles where the polarisation reaches its maximum. Here we present our data, and we use them to estimate the albedo of the object, via semi-empirical formulas that link the albedo to the characteristics of the phase-polarisation curve (e.g., [Cellino et al. 2012, 2016](#)). Additional constraints from spectro-polarimetry also allow us to set some constraints on the spectral class of the asteroid.

2. Observations

We have measured the linear polarisation as a function of wavelength λ and phase angle α

$$P_r(\alpha, \lambda) = \frac{F_\perp - F_\parallel}{F_\perp + F_\parallel} \quad (1)$$

where F_\parallel and F_\perp are the fluxes of the light polarised in the direction parallel or perpendicular to the scattering plane, respectively. In the case of filter polarimetry, λ refers to the effective wavelength of the filter employed in the observations. Consistent with the general description of Sect. 1, a positive sign for P_r means that the light flux polarized perpendicularly to the scattering plane exceeds the flux polarized parallel to it, whereas a negative sign means that the parallel polarization dominates.

Figure 1 shows the observing geometry of FA22 relative to the Earth and Moon in the projected ecliptic x – y (left) and x – z (right) planes during the campaign. The first date of each observing epoch is marked along the asteroid’s path. During the campaign, the NEO passed close to the Earth–Moon system, reaching a minimum geocentric distance of about 842,060 km.

Observations were obtained between 2025-09-18 and 2025-09-28 using both spectropolarimetry and filter polarimetry, covering phase angles from 109° to 24.2° . Data were collected at multiple observatories with different instruments, all employing the beam-swapping technique (e.g., [Bagnulo et al. 2009](#)).

Filter polarimetry was performed with nominally similar B, V, and R filters whose transmission curves differed slightly between instruments. While such differences can be critical in cases where polarisation varies rapidly with wavelength, asteroid polarisation varies smoothly across the optical range – in fact, for FA22, was found also very small. As a result, small differences in filter transmission have a negligible effect compared with photon-noise uncertainties for this target. This assumption was confirmed a posteriori through numerical simula-

tions based on FORS spectropolarimetry combined with different filter transmission functions, and by the agreement, within uncertainties, of observations obtained at nearly identical phase angles with different instruments. Although detailed information on the exact filters is provided in the relevant instrument documentation (see below), we will hereafter refer to the data simply as B, V, and R band observations.

2.1. Filter polarimetry with DIPol-UF

Multicolour filter polarimetry of FA22 was obtained with the Double Image Polarimeter Ultra Fast (DIPol-UF) described by [Pirola et al. \(2021\)](#). This three-channel (B’V’R’) polarimeter is attached to the f/12.5 Cassegrain focus of the Omicron@C2PU telescope (diameter 1.03 m), located at the Calern observing station of Observatoire de la Côte d’Azur, France. The setup involves a super-achromatic half-wave plate (HWP) as the modulator and a plane-parallel calcite plate as the polarising beam splitter. The polarimeter simultaneously records two orthogonally polarised beams from each source in the field of view. Dichroic beam splitters allow for simultaneous recording on three dedicated CCD cameras in B’, V’ and R’ filters. Each cycle involved 16 positions of the retarder plate, and for each position, three images with 90 s exposure time were taken simultaneously by the B’, V’ and R’ cameras. The telescope was in differential tracking mode (following the proper motion of the asteroid). The target’s high proper motion combined with long exposure times yielded long trailed images for the surrounding stars. Thus, some images had to be rejected because of stellar contamination. Data were reduced following the pipeline described by [Pirola et al. \(2021\)](#) and references therein.

2.2. Spectropolarimetry with FORS2

We obtained spectropolarimetric observations of FA22 using the FORS2 instrument ([Appenzeller et al. 1998](#)) on the ESO Very Large Telescope (VLT). FORS2 is a slit-fed spectrograph equipped with a retarder waveplate and a Wollaston prism acting as a beam-splitter polariser. Observations were performed with the 300V grism without using any order-sorting filter, providing spectral coverage between 370 and 930 nm. Slit width was set to 2'', for a spectral resolving power $R \simeq 200$. Data were reduced using the ESO FORS pipeline ([Izzo et al. 2010](#)), supplemented by dedicated Fortran routines. Two frames obtained on 2025-10-18 were discarded in our analysis, due to background star contamination; the polarisation spectra were inconsistent with those obtained in other epochs. Appendix A briefly describes the observations of main-belt asteroids that will be used for comparison in Sect. 4.

2.3. Filter polarimetry with FORS2

In addition to spectropolarimetry, FORS2 was also used to obtain broadband polarimetric measurements, using the R_special and v_high filters. The instrument position angle was aligned to the direction perpendicular to the scattering plane. We measured only the reduced Q/I parameter, setting the retarder waveplate to position angles 0, 45, 90, 135°; observations at the intermediate angles 22.5, 67.5, 112.5 and 157.5° were skipped, as in a reference system aligned with the scattering plane, the U/I parameter is zero for symmetry reasons. Data were reduced as described by [Bagnulo et al. \(2016\)](#) and [Bagnulo et al. \(2023\)](#).

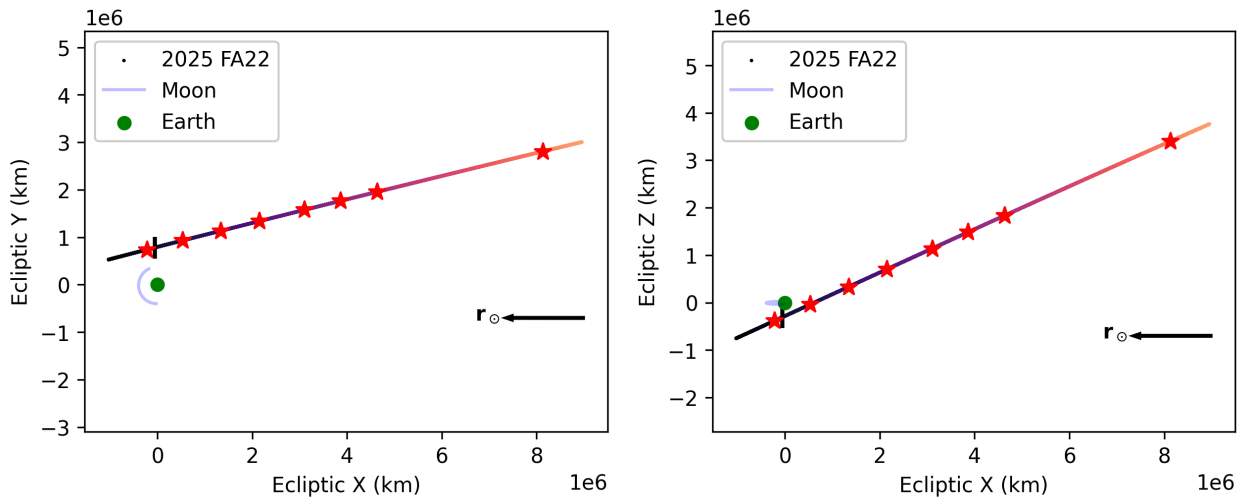


Fig. 1: Observing geometry of FA22 relative to the Moon and Earth in the projected ecliptic x - y (left) and x - z (right) planes. Star symbols mark the UTs of the first observation on each date listed in Table A.1. The vertical bar indicates the projected point at closest Earth approach (UT 2025-09-18T07:39:48.108+00:00; distance $\approx 842,060$ km). The solid black arrow indicates the anti-solar vector at the median epoch of the observing campaign.

2.4. Filter polarimetry with FoReRo2

We also obtained imaging polarimetry in the R_c filter with the two-channel Focal Reducer Rozhen (FoReRo2) (Jockers et al. 2000) attached to the 2-m Ritchey–Chrétien–Coude (2mRCC) telescope of the Bulgarian National Astronomical Observatory (BNAO) Rozhen during four nights in September 2025. When possible, the observations were carried out for 8 retarder angles, but in some cases, to minimise overheads, we used four retarder position angles only. The field of view was generally very crowded, and sometimes the target overlapped the background star trails. For each retarder position angle, we retained three frames in which the asteroid image was not contaminated by star trails.

2.5. Filter polarimetry with ALFOSC

We obtained imaging polarimetric observations in the R_{Bes} and B_{Bes} filters with the Alhambra Faint Object Spectrograph and Camera (ALFOSC) attached to the Nordic Optical Telescope (NOT) during three nights. The polarimetric setup consists of a rotatable retarder waveplate followed by a calcite plate as a beam-splitting device. Observations in each filter consisted of exposures at 16 different retarder waveplate angles. As in the case of FoReRo2, a number of frames were removed due to background star contamination. Data were reduced using dedicated Python scripts.

3. Results

The observing log and the polarisation measurements are given in Table A.1. Polarimetric data were collected in the B, V, and R bands. Although the observations correspond to the same nominal passbands, the specific filters used by each instrument have slightly different transmission functions. For instance, the B filter used by ALFOSC is not identical to the B filter employed by DIPol-UF. Due to the relatively smooth variation of polarisation with wavelength, the specific transmission curves of the filters have only a negligible effect on the measured polarisation, as verified through numerical simulations using FORS2 spectropo-

larimetric data. For simplicity, our results are reported under the generic BVR notation, even though some of the data in the same bands were obtained using distinct filter transmission profiles. The FORS2 spectropolarimetric values of Table A.1 were convolved with the transmission curves of the DIPol-UF filters (see, e.g., Eqs. (19) of Bagnulo et al. 2017).

We have also determined the polarimetric wavelength gradient, or polarimetric colour, defined as

$$PC(\lambda_1, \lambda_2) = \frac{P_r(\lambda_2) - P_r(\lambda_1)}{(\lambda_2 - \lambda_1)}, \quad (2)$$

where $\lambda_2 > \lambda_1$. The polarimetric colours $PC(B,V)$ and $PC(V,R)$ reported in Table A.1 refer to the effective wavelengths of the BVR filters, and are expressed in % per nm.

In the following, we analyse the behaviour as a function of wavelength λ and phase angle α of the quantity $P_r(\alpha, \lambda)$.

3.1. The phase angle polarisation curve and albedo determination

Figure 2 shows the P_r values as a function of the phase-angle. The morphology of these phase-polarisation curves can be characterised by parameters which are linked with important physical characteristics of the object, including the geometric albedo. As mentioned above, because NEAs can be observed at small distances from the Earth, observations can cover much wider intervals of phase angle, as compared with main-belt asteroids.

The behaviour is characterised by a moderately steep polarimetric slope. At phase angles around 50° , P_r reaches values slightly larger than 5% in all filters, suggesting already an albedo value significantly higher than in the case of some low-albedo NEAs, such as (3200) Phaethon (Devogèle et al. 2018).

We computed a best-fit of the data shown in Fig. 2 by using the function

$$P_r(\alpha) = A \sin^B(\alpha) \cos^C\left(\frac{\alpha}{2}\right) \sin(\alpha - \alpha_0) \quad (3)$$

where A , B , C and the inversion phase angle α_0 are parameters to be determined by means of best-fit techniques. Equation (3) is the so-called trigonometric representation of the

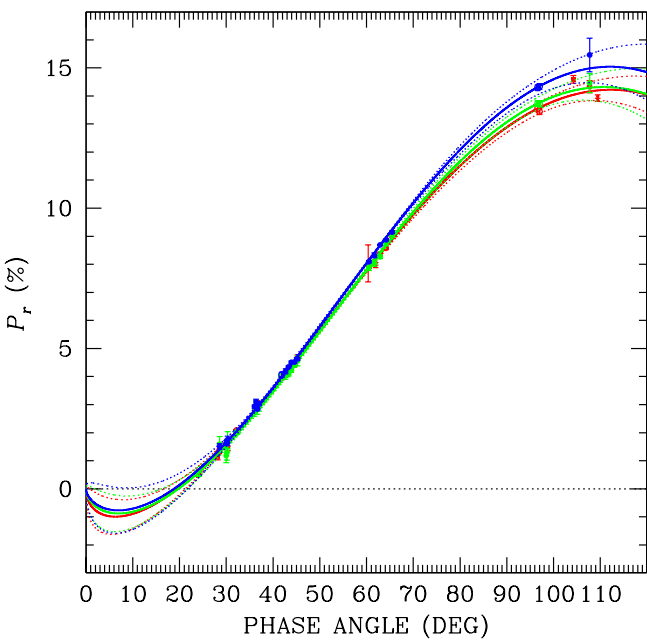


Fig. 2: Phase-polarisation curve. Blue solid circles, green squares and red empty circles refer to the polarisation measurements obtained with the B, V, and R filters, respectively. Solid lines corresponds with the best-fits obtained with Eq. (3) and dotted lines their 3σ boundaries.

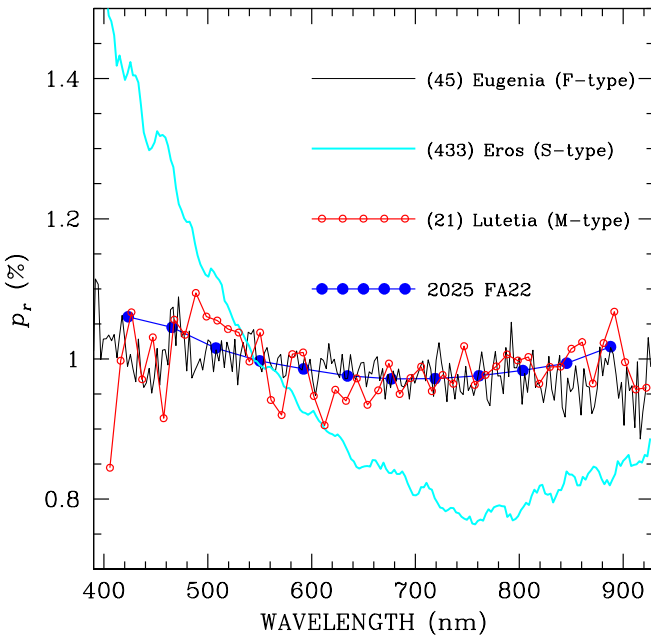


Fig. 3: Normalised polarisation spectrum of 2025 FA22 obtained on 2025-09-18 at $\alpha \simeq 97^\circ$ (blue solid circles) compared with the spectra of other asteroids (obtained in the positive branch).

phase-polarisation relationship of asteroids originally proposed by [Lumme & Muinonen \(1993\)](#), and later adopted by other authors, including, for instance, [Penttila et al. \(2005\)](#) and [Devogèle et al. \(2018\)](#). This representation of the phase-polarisation curve is normally used to fit NEA polarimetric data, because it provides a satisfactory representation of observations obtained up

to high phase angles, well beyond the limits reached by main-belt asteroids.

A Levenberg-Marquardt algorithm allowed us to recover the best-fit values for the A , B , and C parameters, as well as the corresponding covariant matrix. The resulting values for these parameters, as well as for the polarimetric parameters α_0 , P_{\min} , P_{\max} and P_{max} are listed in Table 1. The inversion angle α_0 is nearly independent of wavelength and $\sim 19.5^\circ$.

The next step was to compute analytically the value of the so-called polarimetric slope h , defined as the derivative of $P_r(\alpha)$ computed at the inversion angle α_0 . It is given by

$$h = A \sin^B(\alpha_0) \cos^C\left(\frac{\alpha_0}{2}\right) \quad (4)$$

The resulting value for h in all filters is $\sim 0.12\%/\text{deg}$ (see Table 1). The polarimetric slope h is one of the most important parameters characterising a phase-polarisation curve, as it may be used to feed the semi-empirical relationship that links it to the geometrical albedo a of the object ([Cellino et al. 2015](#) and references therein)

$$\log_{10}(a_{\mathcal{F}}) = C_1 \log_{10}(h_{\mathcal{F}}) + C_2 \quad (5)$$

where $h_{\mathcal{F}}$ is the slope of the curve computed at the inversion angle in the filter \mathcal{F} . In the V filter, the empiric constants are $C_1 = -1.111 \pm 0.031$ and $C_2 = -1.781 \pm 0.025$ ([Cellino et al. 2015](#)), which lead to the estimate of $a_V = 0.16 \pm 0.02$.

3.2. Maximum positive polarisation

Our polarimetric measurements of FA22 allow us to estimate the maximum positive fraction of linear polarisation P_{\max} , a determination that is possible only in rare cases when the object is observed at phase angles up to at least $100 - 110^\circ$. This parameter potentially provides an important constraint for the modelling of the asteroid's surface properties, such as its albedo and grain size ([Ito et al. 2018](#)). Generally, theoretical predictions of P_{\max} can be compared only with laboratory measurements with lunar data, because P_{\max} has been determined only for the Moon and a handful of NEAs. Our polarimetric data of FA22 thus represent an important addition to the observational constraints for modelling work.

3.3. Polarisation versus wavelength

Table A.1 shows that the broadband values are generally quite close to each other, with the polarisation in the B filter slightly higher than in the other filters. This situation is called “blue polarisation”. Figure 3 shows the polarisation spectrum obtained at phase angles $\simeq 97^\circ$, normalised by its values in the V filter (such a normalisation makes the spectrum fairly independent on the phase angle at which it was obtained, see [Bagnulo et al. 2015](#)). The spectrum of FA22 is nearly flat, exhibiting a very mild overall concave shape, with a negative wavelength gradient in the spectral regions covered by the BVR filters ($\lambda \sim 400 - 700$ nm), and a positive wavelength gradient at longer wavelengths ($\lambda \sim 750 - 900$ nm). At its red end, our polarimetric spectrum nearly reaches the same high values as those at its blue end. We note that the full spectrum out to about 0.9 nm reveals a more complex pattern than what the BVR filters alone suggest. This indicates that reliable classification and characterisation of small bodies in the solar system would benefit from spectropolarimetry over a wide wavelength range, ideally extending into the IR.

Table 1: Best-fit coefficients and characteristic parameters of the polarimetric curve, with their 1σ uncertainties. We note that there are no observations in the negative branch, hence the α_{\min} and P_{\min} values are obtained from extrapolation.

Filter	A	B	C	α_0	$(dP_r/d\alpha) _{\alpha=\alpha_0}$	α_{\min}	P_{\min}	α_{\max}	P_{\max}
B	12.540 ± 0.227	0.574 ± 0.108	-0.390 ± 0.044	18.9 ± 1.3	0.12 ± 0.01	6.9 ± 0.3	-0.77 ± 0.27	112.1 ± 2.0	15.04 ± 0.22
V	12.479 ± 0.177	0.543 ± 0.085	-0.308 ± 0.038	19.8 ± 0.8	0.12 ± 0.01	7.0 ± 0.4	-0.88 ± 0.21	110.8 ± 1.8	14.32 ± 0.18
R	12.232 ± 0.147	0.470 ± 0.069	-0.321 ± 0.031	19.6 ± 0.7	0.13 ± 0.01	6.3 ± 0.4	-0.99 ± 0.21	112.3 ± 1.4	14.22 ± 0.14

3.4. Searching for rotational modulation

Rotational modulation of asteroid polarisation is rarely observed, which suggests that surface structure usually does not vary enough to produce detectable changes at small phase angles. A clear exception is Vesta, where ultra-precise measurements revealed such variability (Wiktorowicz & Nofi 2015; Cellino et al. 2016). NEAs offer better chances because they can be observed at large phase angles, where the intrinsic polarisation is higher and potential variations stand out more clearly (Borisov et al. 2018; Devogèle et al. 2024). For FA22, however, we found no evidence of rotational modulation.

4. Comparison with other asteroids

The polarisation spectrum of FA22 resembles the nearly wavelength-independent behaviour shown by some C-class asteroids reported by Kwon et al. (2023). This similarity, however, does not imply a compositional link. The Umov law (Umov 1905) tells us that polarimetric spectra often track the inverse of reflectance spectra. Within any taxonomic class the range of spectral slopes can be wide. C-type asteroids, for example, span steep, moderate, and nearly flat reflectance slopes (DeMeo et al. 2009). Their inverse trends differ accordingly. Because of this variability, matching FA22 to any specific C-type asteroid would be unreliable. FA22 lacks the low albedo typical of the C-class, typically well below 0.08, and its polarisation phase curve does not show the steep behaviour expected for that group.

Figure 3 shows a striking resemblance between the polarisation spectrum of FA22 and that of main-belt F-class asteroid (45) Eugenia. However, the inversion angle of the polarisation curve of FA22, $\alpha_0 \sim 20^\circ$ is typical of the large majority of the main-belt asteroids. This rules out a link to other classes of low-albedo asteroids, including B and, more markedly, F, which exhibit α_0 values below 20° (Belskaya et al. 2017). Moreover, a few of these asteroids reach values of $P_{\max} \gtrsim 40\%$ (B-type asteroid 3200 Phaeton; Devogèle et al. 2018), or exceed 20% already at phase angle $\sim 50^\circ$ (F-type asteroid 101955 Bennu; Cellino et al. 2018), well above what we measure for FA22. We can also exclude asteroids with unusually large inversion angles, such as the Barbarians, which show $\alpha_0 > 30^\circ$ (e.g., Cellino et al. 2006, 2018).

The albedo of FA22 is only marginally consistent with that of several S-class asteroids. These objects, though, show a slope reversal in their polarisation spectra, which occurs at longer wavelengths than in FA22. (Their reversal appears near 760 nm, while FA22 shows a minimum near 700 nm). The polarimetric slopes of S-class are also much steeper than those measured here, both where the gradient is positive and where it is negative (see, as an example the polarimetric spectrum of the S-class NEA (433) Eros shown in Fig. 3). Furthermore, S-types reach at most $P_{\max} \simeq 7 - 8\%$ (Ishiguro et al. 2017; Kiselev et al. 2024; Shcherbina et al. 2025), much lower than the value for FA22.

An interesting fact is the resemblance of some polarimetric properties of FA22 with those for the lunar highlands, e.g., they have similar albedo, characteristics of the polarisation minimum, value of P_{\max} ; also, some young features demonstrate similar wavelength behaviour of polarisation (Shkuratov et al. 2015). However, they differ in the inversion angle and location of the maximum.

Although the problem of finding asteroidal analogues of the polarimetric spectrum of FA22 seems to be difficult, We note that there is a clear similarity with the polarimetric spectrum of the large (about 100 km in diameter) asteroid (21) Lutetia, originally a member of the Tholen M class (Tholen 1984) and later reclassified as Xc in the SMASS system (Bus & Binzel 2002; DeMeo et al. 2009). Xc asteroids typically show almost flat reflectance and polarisation spectra (Bagnulo et al. 2015), and some exhibit $\alpha_0 \sim 20^\circ$ (Cañada-Assandri et al. 2012).

The polarimetric spectrum of Lutetia is displayed as a red line in Fig. 3, and it is easy to see that its spectrum fits quite well the polarisation spectrum of FA22. According to current knowledge, (21) Lutetia and FA22 share also comparable albedos, but their phase polarisation curves exhibit some relevant differences. Lutetia inverts near 25° (Cellino et al. 2016), while FA22 does so around 20° .

(21) Lutetia's former taxonomic classification is interesting, because M class asteroids were long thought to be metal rich (Matter et al. 2013). The spectroscopic survey of M types by Fornasier et al. (2010) shows a wide range of reflectance slopes whose shapes resemble the inverse of FA22's polarisation spectrum. This makes an M type assignment plausible. Belskaya et al. (2022) conducted a general investigation of the polarimetric properties of asteroids that had been originally assigned to the M taxonomic class. They found that, when looking at the relationship between the depth of the negative polarisation branch and the inversion angle, they could subdivide M-class asteroids into two main sub-types, possibly related to different surface compositions. One subgroup seems to be similar to irons and stony-iron meteorites, while the second subgroup, which includes (21) Lutetia, seems to be more similar to enstatite and iron-rich carbonaceous chondrites.

5. Conclusions

After earlier NEA polarimetric observations collected between 2020 and 2023 within the NEOROCKS project,² these new observations of FA22 represent one of the most extensive and systematic polarimetric studies of a NEA at large phase angles. Although they sample only the positive polarisation branch, the data are dense and accurate enough to determine the key polarimetric parameters, including the inversion angle α_0 , the polarimetric slope h , and the maximum positive polarisation P_{\max} , reached at a phase angle of about 110° . We also obtained the

² see <https://www.neorocks.eu/>

first spectro-polarimetric measurements of a small Solar System body near its polarisation maximum. No convincing evidence is found for surface heterogeneity producing measurable polarimetric effects.

These results constrain the surface properties of FA22 and provide a valuable test case for rapid-response polarimetric techniques applied to newly discovered NEAs. We derive an albedo of 0.16 ± 0.02 , intermediate between typical *C*-class and *S*-complex asteroids. This value, together with the polarisation spectrum, is consistent with some M-type asteroids. Combined with forthcoming photometric measurements of the absolute magnitude of FA22, this albedo will allow an estimate of the object's size.

Acknowledgements. Based on observations obtained with data collected at the Paranal Observatory under programs ID 115.29F0.002 and 115.29F0.003 (filter polarimetry and spectro polarimetry of FA22, PI Ieva), 095.C-0925(A) (spectropolarimetry of Lutetia and Eugenia, PI=Bagnulo) and 092.C-0639(A) (spectropolarimetry of Eros, PI=Cellino). G.B. acknowledges partial support from grant K11-06-H88/5 by the Bulgarian National Science Fund. G.B. gratefully acknowledges observing grant support from the Institute of Astronomy and the National Astronomical Observatory, Bulgarian Academy of Sciences. BNAO Rozhen is a facility of the National Roadmap for Research Infrastructure 2020-2027 (RACIO project), financially coordinated by the Ministry of Education and Science of the Republic of Bulgaria. S.V.B. acknowledges the support of the ERC Advanced Grant HotMol ERC-2011-AdG-291659 for the construction of the DIPol-UF polarimeter, in collaboration with the University of Turku, Finland. This project is funded by the Horizon Europe Programme of the European Union and implemented by ESA. Views and opinion expressed are however those of the authors only and the European Commission cannot be held responsible for any use which may be made of the information contained therein.

Lumme, K. & Muinonen, K. 1993, in Abstracts for the IAU Symposium 160: Asteroids, Comets, Meteors 1993, ed. A. Milani, M. Di Martino, & A. Cellino, 194

Matter, A., Delbo, M., Carry, B., & Ligori, S. 2013, Icarus, 226, 419

Penttila, A., Lumme, K., Hadamicic, E., & Levasseur-Regourd, A.-C. 2005, \AA , 432, 1081

Piirola, V., Kosenkov, I. A., Berdyugin, A. V., Berdyugina, S. V., & Poutanen, J. 2021, AJ, 161, 20

Shcherbina, M. P., Kiselev, N. N., Karpov, N. V., & Zhuzhulina, E. A. 2025, Solar System Research, 59, 61

Shkuratov, Y., Opanasenko, N., Korokhin, V., & Videen, G. 2015, in Polarimetry of Stars and Planetary Systems, ed. L. Kolokolova, J. Hough, & A.-C. Levasseur-Regourd, 303

Tholen, D. J. 1984, PhD thesis, University of Arizona

Umov, N. A. 1905, Phis. Zeits., 6, 674–676

Wiktorowicz, S. J. & Nofi, L. A. 2015, ApJ, 800, L1

References

Appenzeller, I., Fricke, K., Fürtig, W., et al. 1998, The Messenger, 94, 1

Bagnulo, S., Belskaya, I., Cellino, A., et al. 2024, The Astronomy and Astrophysics Review, 32, 7

Bagnulo, S., Belskaya, I., Stinson, A., Christou, A., & Borisov, G. B. 2016, A&A, 585, A122

Bagnulo, S., Cox, N. L. J., Cikota, A., et al. 2017, A&A, 608, A146

Bagnulo, S., Fossati, L., Landstreet, J. D., & Izzo, C. 2015, A&A, 583, A115

Bagnulo, S., Gray, Z., Granvik, M., et al. 2023, ApJ, 945, L38

Bagnulo, S., Landolfi, M., Landstreet, J. D., et al. 2009, PASP, 121, 993

Belskaya, I., Fornasier, S., Tozzi, G., et al. 2017, Icarus, 284, 30

Belskaya, I. N., Berdyugin, A., Krugly, Y., et al. 2022, \AA , 663

Borisov, G., Devogèle, M., Cellino, A., et al. 2018, MNRAS, 480, L131

Bus, S. J. & Binzel, R. P. 2002, Icarus, 158, 146

Cañada-Assandri, M., Gil-Hutton, R., & Benavidez, P. 2012, A&A, 542, A11

Cellino, A., Ammannito, E., Magni, G., et al. 2016, MNRAS, 456, 248

Cellino, A., Bagnulo, S., Belskaya, I. N., & Christou, A. A. 2018, MNRAS, 481, L49

Cellino, A., Bagnulo, S., Gil-Hutton, R., et al. 2015, MNRAS, 451, 3473

Cellino, A., Bagnulo, S., Gil-Hutton, R., et al. 2016, Monthly Notices of the Royal Astronomical Society, 455, 2091

Cellino, A., Belskaya, I. N., Bendjoya, P., et al. 2006, Icarus, 180, 565

Cellino, A., Gil-Hutton, R., Dell'Oro, A., et al. 2012, Journal of Quantitative Spectroscopy and Radiative Transfer, 113, 2552

DeMeo, F. E., Binzel, R. P., Slivan, S. M., & Bus, S. J. 2009, Icarus, 202, 160

DeMeo, F. E., Binzel, R. P., Slivan, S. M., & Bus, S. J. 2009, Icarus, 202, 160

Devogèle, M., Cellino, A., Borisov, G., et al. 2018, MNRAS, 479, 3498

Devogèle, M., McGilvray, A., MacLennan, E., et al. 2024, The Planetary Science Journal, 5, 44

Fornasier, S., Clark, B. E., Dotto, E., et al. 2010, Icarus, 210, 655

Ishiguro, M., Kuroda, D., Watanabe, M., et al. 2017, AJ, 154, 180

Ito, T., Ishiguro, M., Arai, T., et al. 2018, Nature Communications, 9, 2486

Izzo, C., de Bilbao, L., Larsen, J., et al. 2010, in Society of Photo-Optical Instrumentation Engineers (SPIE) Conference Series, Vol. 7737, Observatory Operations: Strategies, Processes, and Systems III, ed. D. R. Silva, A. B. Peck, & B. T. Soifer, 773729

Jockers, K., Credner, T., Bonev, T., et al. 2000, Kinematika i Fizika Nebesnykh Tel Supplement, 3, 13

Kiselev, N. N., Savushkin, A. A., Petrov, D. V., et al. 2024, MNRAS, 527, 3174

Kwon, Y., Bagnulo, S., & Cellino, A. 2023, \AA , 677, A146

Appendix A: Observing log of the polarimetric measurements

Table A.1: Observing log. FORS2 observations in spectropolarimetric mode (PMOS) are reported giving the polarisation values convolved with the response curves of the filters used in the DIPol-UF instrument. FORS2 (IPOL) refers to VLT measurements obtained with filter polarimetry.

Date YYYY-MM-DD	UT hh:mm	Exp (s)	α ($^{\circ}$)	P_r (%)			$PC(B,V)$ (% per nm)	$PC(V,R)$ (% per nm)	Instrument
				B	V	R			
2025-09-18	02:49	1440	109.43			13.92 \pm 0.12			FoReRo2
2025-09-18	03:42	2880	107.47	15.46 \pm 0.60	14.02 \pm 0.35	14.33 \pm 0.22	-0.0152 \pm 0.0073	+0.0031 \pm 0.0041	DIPol
2025-09-18	05:09	440	104.24	14.88 \pm 0.16		14.59 \pm 0.14			ALFOSC
2025-09-18	08:16	240	96.98	14.33 \pm 0.10	13.71 \pm 0.10	13.44 \pm 0.10	-0.0065 \pm 0.0015	-0.0027 \pm 0.0014	FORS2 (PMOS)
2025-09-18	08:26	240	96.58	14.29 \pm 0.10	13.73 \pm 0.10	13.54 \pm 0.10	-0.0059 \pm 0.0015	-0.0019 \pm 0.0014	FORS2 (PMOS)
2025-09-18	23:55	2880	65.49	9.15 \pm 0.05	9.04 \pm 0.05	9.00 \pm 0.04	-0.0012 \pm 0.0007	-0.0004 \pm 0.0006	DIPol
2025-09-19	00:47	2880	64.20	8.87 \pm 0.04	8.72 \pm 0.05	8.57 \pm 0.04	-0.0016 \pm 0.0007	-0.0015 \pm 0.0006	DIPol
2025-09-19	01:41	2880	62.89	8.69 \pm 0.10	8.27 \pm 0.07	8.37 \pm 0.07	-0.0044 \pm 0.0013	+0.0010 \pm 0.0010	DIPol
2025-09-19	02:18	720	61.95			7.97 \pm 0.09			FoReRo2
2025-09-19	02:32	2880	61.68	8.32 \pm 0.09	8.04 \pm 0.11	8.09 \pm 0.05	-0.0029 \pm 0.0015	-0.0005 \pm 0.0012	DIPol
2025-09-19	03:25	2880	60.50	8.09 \pm 0.04	7.88 \pm 0.10	7.89 \pm 0.04	-0.0022 \pm 0.0011	+0.0001 \pm 0.0011	DIPol
2025-09-19	03:38	40	60.34			8.03 \pm 0.66			ALFOSC
2025-09-19	21:49	4320	45.27	4.63 \pm 0.05	4.56 \pm 0.18	4.70 \pm 0.07	-0.0007 \pm 0.0020	+0.0014 \pm 0.0019	DIPol
2025-09-19	23:07	4320	44.58	4.51 \pm 0.04	4.44 \pm 0.11	4.40 \pm 0.04	-0.0007 \pm 0.0012	-0.0004 \pm 0.0012	DIPol
2025-09-20	00:22	4320	43.93	4.51 \pm 0.04	4.23 \pm 0.08	4.38 \pm 0.06	-0.0029 \pm 0.0009	+0.0015 \pm 0.0010	DIPol
2025-09-20	01:38	4320	43.30	4.34 \pm 0.04	4.07 \pm 0.05	4.27 \pm 0.05	-0.0028 \pm 0.0007	+0.0020 \pm 0.0007	DIPol
2025-09-20	02:39	1440	42.77			4.06 \pm 0.05			FoReRo2
2025-09-20	02:53	4320	42.71	4.19 \pm 0.09	4.03 \pm 0.13	4.04 \pm 0.04	-0.0017 \pm 0.0017	+0.0001 \pm 0.0014	DIPol
2025-09-20	05:28	240	41.85	4.06 \pm 0.10	3.99 \pm 0.10	3.98 \pm 0.10	-0.0007 \pm 0.0015	-0.0001 \pm 0.0014	FORS2 (PMOS)
2025-09-20	21:14	6120	37.01	3.03 \pm 0.07	2.92 \pm 0.15	3.00 \pm 0.09	-0.0012 \pm 0.0017	+0.0008 \pm 0.0017	DIPol
2025-09-20	21:33	1440	36.92			2.95 \pm 0.05			FoReRo2
2025-09-20	22:43	6120	36.67	2.84 \pm 0.03	2.83 \pm 0.18	3.04 \pm 0.10	-0.0001 \pm 0.0019	+0.0021 \pm 0.0021	DIPol
2025-09-21	00:00	6120	36.37	3.10 \pm 0.09	3.00 \pm 0.16	2.90 \pm 0.10	-0.0011 \pm 0.0018	-0.0010 \pm 0.0019	DIPol
2025-09-21	01:16	6120	36.08	2.93 \pm 0.06	2.77 \pm 0.19	2.91 \pm 0.06	-0.0017 \pm 0.0020	+0.0014 \pm 0.0019	DIPol
2025-09-22	03:40	28	32.20			2.07 \pm 0.04			FORS2 (IPOL)
2025-09-22	03:44	40	32.19		2.00 \pm 0.05		+0.0007 \pm 0.0006		FORS2 (IPOL)
2025-09-22	22:09	6120	30.31	1.75 \pm 0.12	1.73 \pm 0.31	1.52 \pm 0.16	-0.0002 \pm 0.0035	-0.0021 \pm 0.0035	DIPol
2025-09-22	23:55	6120	30.16	1.63 \pm 0.08	1.30 \pm 0.28	1.64 \pm 0.10	-0.0035 \pm 0.0030	+0.0034 \pm 0.0029	DIPol
2025-09-23	01:41	6120	30.00	1.63 \pm 0.09	1.19 \pm 0.26	1.55 \pm 0.09	-0.0046 \pm 0.0029	+0.0036 \pm 0.0028	DIPol
2025-09-23	22:02	3240	28.58	1.51 \pm 0.10	1.59 \pm 0.27	1.42 \pm 0.11	+0.0008 \pm 0.0030	-0.0017 \pm 0.0029	DIPol
2025-09-24	03:36	60	28.30			1.29 \pm 0.04			FORS2 (IPOL)
2025-09-24	04:14	2400	28.19	1.30 \pm 0.09		1.16 \pm 0.13			ALFOSC
2025-09-28	03:59	80	24.17			0.60 \pm 0.07			FORS2 (IPOL)
2025-09-28	04:05	100	24.17		0.52 \pm 0.07		+0.0008 \pm 0.0010		FORS2 (IPOL)

Minor Planet Center (MPC) observatory codes are as follow. DIPol@C2PU (Calern): R87; FORS2@VLT (Cerro Paranal): 309; FoReRo2@2mRCC (Rozhen): 071; ALFOSC@NOT (La Palma): Z23.

Appendix B: Observations and data reduction of main-belt asteroids

Spectropolarimetric observations of main-belt asteroids of Fig. 3 were obtained with FORS2 at the ESO VLT with 300 V grism and a 2 " slit width, using the same technique briefly summarised in Sect. 2.2 (see also [Bagnulo et al. 2015](#)). The spectrum of asteroid (433) Eros was obtained on 2014-02-15 at $\alpha = 42.0^\circ$, and already published by [Bagnulo et al. \(2015\)](#); that of (45) Eugenia was obtained on 2015-06-18 at $\alpha = 21.8^\circ$, and that of (21) Lutetia was obtained on 2015-06-02 at $\alpha = 27.5^\circ$. Figure 3 shows these spectra normalised to their values at 550 nm.